Individual-atom control in an array through phase modulation

Guoqing Wang (王国庆), [1,2,3,*,§] Wenchao Xu, [4,5,§] Changhao Li, [1,2] Vladan Vuletić, [1,3,†] and Paola Cappellaro [1,2,3,‡]

[1] MIT-Harvard Center for Ultracold Atoms and Research Laboratory of Electronics, Massachusetts Institute of Technology, Cambridge, Massachusetts 02139, USA
[2] Department of Nuclear Science and Engineering, Massachusetts Institute of Technology, Cambridge, Massachusetts 02139, USA
[3] Department of Physics, Massachusetts Institute of Technology, Cambridge, Massachusetts 02139, USA
[4] Department of Physics/Institute of Quantum Electronics and Quantum Center, ETH Zürich, 8093 Zürich, Switzerland
[5] Laboratory for Nano and Quantum Technologies, Paul Scherrer Institut, 5232 Villigen PSI, Switzerland

(Received 30 November 2023; revised 21 September 2024; accepted 30 January 2025; published 28 February 2025)

Performing parallel-gate operations while retaining low crosstalk is an essential step in transforming neutral-atom arrays into powerful quantum computers and simulators. Tightly focusing control beams in small areas for crosstalk suppression is typically challenging and can lead to imperfect polarization for certain transitions. We tackle such a problem by introducing a method to engineer single-qubit gates through phase-modulated continuous driving. Distinct qubits can be individually addressed to high accuracy by simply tuning the modulation parameters, which significantly suppresses crosstalk effects. When arranged in a lattice structure, optimal crosstalk suppression can be achieved by choosing the appropriate modulation parameters. With the assistance of additional addressing light or multiple modulation frequencies, we develop two parallel-gate schemes with efficient and easy experimental implementations compared to existing light-shift methods. Our results pave the way to scaling up atom-array platforms and achieving individual-atom control of a three-dimensional array with low-error parallel-gate operations, without requiring complicated wavefront design or high-power laser beams.

DOI: 10.1103/PhysRevApplied.23.024072

I. INTRODUCTION

Arrays of individual atoms trapped in optical tweezers have emerged as an attractive architecture for implementing quantum computation and simulation [1,2]. Current state-of-the-art atom-array platforms have achieved global single-qubit operation with 99.99% fidelity and two-qubit gate operation with 99.5% fidelities [3–8]. Still, performing scalable, arbitrary local gate operations over a subset of atoms inside an atom array without crosstalk is an outstanding challenge. The generation of arrays of rapidly switchable and reconfigurable laser beams that can address atoms individually is a demanding task for optical modulators, especially in view of the requirements on maintaining the intensity and frequency of these laser beams.

Currently, there exist two major strategies for performing local qubit operations. The first one relies on transporting atoms either into a separated manipulation region where many target atoms are addressed by global beams [9] or using subwavelength controlled moves on individual atoms to induce a position-dependent phase imprinted by a global control beam [10]. The transport time in this approach unavoidably scales up with the system size. To avoid atom shuttling, an alternative strategy is to introduce local beams to apply operations such as light shift [11–14], Raman control [5,15], and Rydberg gates [16] to only a subset of atoms. A large detuning and a high power are usually preferred to reduce crosstalk and suppress the error rate due to light scattering. Tightly focusing local addressing beams aligns with these goals while bringing new challenges of eliminating the position fluctuations of the beams, especially when the distance between atoms is small. Furthermore, it becomes more challenging to maintain perfect polarization for these tightly focused beams, which are required for reliable control over atomic transitions.

To overcome the challenges of locally controlling optical transitions within atom-array-based architecture, it would be helpful to develop a control scheme that uses a larger beam waist while simultaneously suppressing deleterious effects. In this work, we develop a novel

*Contact author: gq_wang@mit.edu
†Contact author: vuletic@mit.edu
‡Contact author: pcappell@mit.edu
§These authors contributed equally to this work.

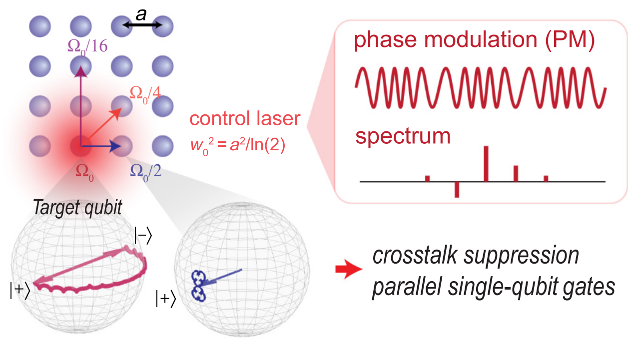

FIG. 1. Low-crosstalk gates in atom arrays. By modulating the phase of a loosely focused local addressing beam, a rotational gate is applied to the target atom while deeply suppressing the crosstalk on nearby atoms. The evolution trajectories on Bloch spheres showcase a crosstalk-suppressed Z gate for the target and nearby atoms.

scheme to implement parallel single-qubit gate operations on the target qubits while suppressing crosstalk effects due to power leakage on the rest of the qubits. By engineering a phase-modulated concatenated continuous driving, the desired quantum gate is selectively applied to the target qubit, while the rest experience identity operations. As shown in Fig. 1, for atom arrays arranged in a lattice structure, significant crosstalk suppression can be achieved by properly choosing the spacing between optical tweezers. Based on such a technique, we further propose two new schemes to achieve parallel-gate operations on a subset of atoms by either tuning Rabi frequencies with additional light-shift beams to prevent the atom from being driven, or adding multiple modulation frequencies to target different sites simultaneously. Our method does not require using a far-detuned high-power laser to apply ac Stark shifts to qubit levels. It paves the way to achieving large-scale quantum computation with low-error parallel-gate operations, and can be used for three-dimensional arrays of atoms, for which existing techniques are not suitable.

II. CONSTRUCTING A LOW-CROSSTALK GATE USING PHASE MODULATION

A variety of control techniques have been exploited to engineer quantum gates in the presence of control constraints. The most-studied approach for protecting a quantum operation against these limitations are composite pulses [17], which combine several imperfect pulses to construct an operation with smaller error [18–20]. Tailored to different applications, composite pulses can be designed to have broadband, narrowband, or passband features [21,22], and can be made robust to nonunitary errors [23,24]. Based on available primitive gates, a systematic and efficient methodology for composite gate design has been developed [25] and some efforts have also been devoted to improving the smoothness of the temporal shape [26,27]. In atom-array quantum platforms, composite pulses or similar optimal control approaches have been applied to improve the quantum gate performance [6,7,28].

However, the errors arising in local gate operations within atom arrays are distinct from many of the situations that have been previously addressed, and thus call for new solutions. The crosstalk in atom-array systems is predominantly induced by the leakage of the laser power to neighboring qubits due to the finite focal size of the laser beam. Such an issue originates from a dilemma on the choice of beam waist: while a very small beam waist is preferred to reduce the crosstalk with nearby atoms, it raises challenges in maintaining position stability and polarization purity. In contrast to previous methods that introduce additional tightly focused addressing light beams to differentiate target qubits and suppress crosstalk, here we propose to eliminate crosstalk by engineering the global phase of the control beam, exploiting so-called *concatenated continuous driving* (CCD), which was previously developed to protect qubit coherence [29–33] and design optimal control pulses in solid-state systems [34,35].

The phase modulation (PM) applied to the control field is described by the following single-qubit Hamiltonian:

$$\mathcal{H}_{PM} = \frac{\omega_0}{2}\sigma_z + \Omega\cos\left(\omega t + \phi - \frac{2\epsilon_m}{\omega_m}\sin(\omega_m t + \phi_m)\right)\sigma_x, \tag{1}$$

where ω is set to the qubit frequency ω_0, $\Omega = \Omega(r)$ is the spatially varying driving strength, and ϵ_m, ω_m, and ϕ_m are spatially independent modulation parameters. In the rotating frame defined by

$$U = \exp\left[-i\left(\frac{\omega t}{2}\sigma_z - \epsilon_m\frac{\sin(\omega_m t + \phi_m)}{\omega_m}\sigma_z\right)\right],$$

the Hamiltonian $\mathcal{H}_I = U^\dagger\mathcal{H}_{PM}U - U^\dagger i(dU/dt)$ is

$$\mathcal{H}_I = \frac{\Omega}{2}\sigma_x' + \epsilon_m\cos(\omega_m t + \phi_m)\sigma_z, \tag{2}$$

where $\sigma_x' = \sigma_x\cos\phi + \sigma_y\sin\phi$.

We note that this Hamiltonian can be made time-independent by transforming to a second interaction picture (rotating) frame defined by $\omega_m\sigma_x'/2$ and taking the weak modulation approximation, or rotating-wave approximation (RWA) ($\epsilon_m \ll \omega_m$). We then obtain the Hamiltonian

$$\mathcal{H}_{I,2} = \frac{\Omega - \omega_m}{2}\sigma_x' + \frac{\epsilon_m}{2}\sigma_z', \tag{3}$$

where $\sigma_z' = \cos\phi_m\,\sigma_z - \sin\phi_m\,\sigma_y'$.

Consider, for example, the goal of applying a rotation of angle φ about the z axis. Our scheme implements this by driving a φ rotation in the second rotating frame.

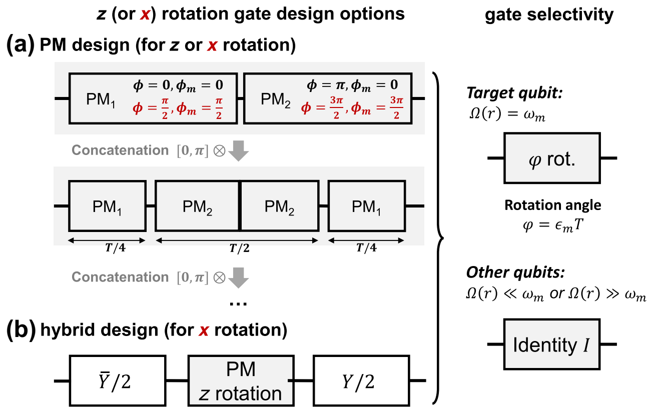

FIG. 2. Single-qubit rotation gate design. Each block represents the application of the phase modulation (PM) drive with the specified phases ϕ and ϕ_m. For rotations along x, a hybrid design option combines a PM z rotational gate with bare $\pi/2$ rotations along y and $-y$, denoted as $Y/2$ and $\bar{Y}/2$ gates.

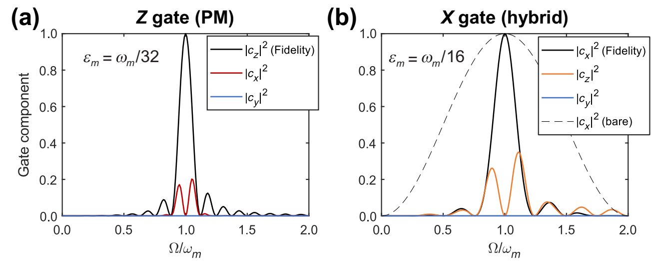

FIG. 3. Gate performance. (a) Fidelity of the PM design Z gate [PM1-PM2-PM2-PM1, same for (b)] as a function of Rabi frequency normalized by the modulation frequency Ω/ω_m. (b) Fidelity of the hybrid design X gate as a function of Rabi frequency.

We set the modulation frequency to the resonance condition $\omega_m = \Omega$ and the modulation phase $\phi_m = 0$ such that $\sigma_z' = \sigma_z$. By further setting the modulation amplitude to $\epsilon_m = \omega_m\varphi/(2\pi k)$, with k any positive integer, a φ rotation along z is achieved for a total evolution time $T = \varphi/\epsilon_m$. Furthermore, the (second) rotating frame transformation is an identity operation as $\omega_m T = 2\pi k$; thus a φ rotation along z is also applied in the first rotating frame.

As illustrated in Fig. 1, with a large size control beam illuminating the array, atoms experience different Rabi frequency Ω due to the spatially dependent light intensity. Our method manifests its advantage in its selectivity by targeting the resonance condition $\Omega = \omega_m$, which is equivalent to selecting the target qubit based on the spatial variation of Ω. Besides the target qubit, other qubits are expected to undergo an identity operation under the applied control. This is because the actual rotation is along a direction close to x' at a rate $\sqrt{(\Omega-\omega_m)^2+\epsilon_m^2}$, since $|\Omega-\omega_m| \gg \epsilon_m$. Such an evolution can be simply canceled by alternating between $\phi = 0$ (giving $\sigma_x' = \sigma_x$) and $\phi = \pi$ (giving $\sigma_x' = -\sigma_x$) in the two halves of the total evolution duration, which gives an effective identity operation [see Fig. 2(a)].

Similar designs can engineer single-qubit rotation gates along other directions by tuning the modulation phases ϕ and ϕ_m. To engineer rotations along x, we can set the modulation phase $\phi_m = \pi/2, 3\pi/2$ and $\phi = \pi/2, 3\pi/2$ for the two halves of the evolution, such that the total rotation is along $\sigma_z' = \sigma_y' = \sigma_x$. An improved design achieves a better crosstalk suppression at small power leakage: this so-called *hybrid design* interleaves the PM-designed z rotation in between two bare $\pi/2$ rotations about y or $-y$ [$Y/2$ and $\bar{Y}/2$ gates in Fig. 2(b)] [15,36–38].

Using Z (PM design) and X (hybrid design) gates as examples, we numerically simulate the evolution $U = \mathcal{T}\exp\{-i\int H_I(t)\,dt\}$ in the first rotating frame, where $\mathcal{T}$ is the time ordering operator, since $H_I(t)$ at different times t does not commute. Decomposing U as $U = c_0 I + c_x\sigma_x + c_y\sigma_y + c_z\sigma_z$, we plot the values of $|c_x|^2$, $|c_y|^2$, and $|c_z|^2$ as functions of Ω/ω_m, which characterize the crosstalk effect. The values at $\Omega/\omega_m = 1$ indicate the gate performance for the target qubit, which shows high-fidelity Z and X operations in Figs. 3(a) and 3(b), respectively. For the rest of the qubits with $\Omega/\omega_m \ll 1$, crosstalk effects for the X gate are suppressed in comparison to the bare X gate without PM (dashed line).

The principle of our selective operation strategy is similar to the light-shift-based method in the sense that the driving term is on-resonance with the target qubit and off-resonance with the spectator qubits. In light-shift methods, the induced energy shift $\Omega^2_{\text{addressing}}/\Delta$ is second-order-dependent on the drive amplitude, and the Rabi frequency Ω of the single-qubit gate should be much smaller than the energy shift. In our method, the effective "energy shift" $(\Omega-\omega_m)$ is linearly dependent on the drive amplitude Ω (Rabi frequency) through the first-order coupling. The bandwidth of the designed gate is then set by the modulation amplitude ϵ_m, as shown in Figs. 3(a) and 3(b). To suppress crosstalk effects, ϵ_m should be much smaller than the "energy shift" $|\omega_m - \Omega|$ for spectator qubits [see Eq. (3)].

Leveraging the periodic zero-crossing feature of the gate components shown in Figs. 3(a) and 3(b), one can arrange atom arrays into special spatial patterns to achieve even better suppression performance. When the atoms are arranged in a square lattice, as shown in Fig. 1, the crosstalk effects can be optimally suppressed by setting the radius r_0 of the Rabi frequency spatial profile $\Omega(r) \propto e^{-r^2/r_0^2}$ (applied by a Gaussian laser beam) to $a = r_0\sqrt{\ln 2}$, where a is the lattice constant. Under this condition, the nearest neighbor has one half of the driving amplitude while the second nearest neighbor has a quarter in comparison to the target qubit, and gate amplitudes (x, y, z rotation components) at these sites are zero, as shown in the simulation in Figs. 3(a) and 3(b), indicating optimal crosstalk suppression performance.

III. PARALLEL CONTROL SCHEMES

A. Parallel control of hyperfine qubits with additional light shifts

Until now we have introduced a phase-modulated control scheme over general two-level systems, which directly applies to optical qubits manipulated by single-photon transitions. For hyperfine qubits addressed via two-photon Raman transitions, our scheme can be applied by phase modulating the frequency difference between the two lights with an electro-optic modulator. Moreover, with the assistance of additional individual-addressing light, as shown in Fig. 4(a), we show in the following that our scheme can be extended to implement parallel single-qubit operations over a selective subset of atomic hyperfine qubits.

Let us consider a Z gate engineered through a two-photon process by two global laser beams, as shown in Fig. 4(a) with a (two-photon) Rabi frequency $\Omega_{\text{eff}} = \Omega_1\Omega_2/(2\Delta)$. Off-resonant addressing beams are applied on the target qubit, e.g., using acousto-optic deflectors (AODs) or spatial light modulators (SLMs), and digital micromirror devices (DMDs) [39]. These addressing beams mix the intermediate state with a fourth state to change the effective detuning in the two-photon transition, thus modifying the Rabi frequency of the hyperfine qubit. Combined with the selectivity of the target operations over the Rabi frequency, the target operations are then applied to atoms with (or without) addressing beams, while identity operations are applied to the spectators. With the periodic zero-crossing spectrum feature, the additional light shifts only need to change the effective Rabi frequency by an amount on the order of $\sim\epsilon_m$ instead of Ω, reducing the power requirement on the addressing beams.

More quantitatively, in the rotating frame defined by the drive frequencies, the system can be described by a four-level Hamiltonian

$$H = -\Delta\,|e\rangle\langle e| - (\Delta + \Delta_c)\,|s\rangle\langle s| + [\Omega_1\,|\uparrow\rangle\langle e| + \Omega_2\,|\downarrow\rangle\langle e| + \Omega_c\,|e\rangle\langle s| + \text{H.c.}]/2,$$

with $|\downarrow\rangle$ and $|\uparrow\rangle$ denoting the qubit states, and $|e\rangle$ and $|s\rangle$ denoting the intermediate and additional states. When $\Delta, \Delta - \Delta_c \gg \Omega_1, \Omega_2$, we can adiabatically eliminate the two excited states $|e\rangle$ and $|f\rangle$ and simplify the Hamiltonian to the qubit subspace (see Appendix B for details). The effective Rabi rate between the qubit states is

$$\Omega_{\text{eff}} = \frac{\Omega_1\Omega_2}{2\Delta - \Omega_c^2/[2(\Delta + \Delta_c)]}. \tag{4}$$

To modify the effective Rabi rate by a factor of α, we can choose the detuning as $\Delta_c = -\Delta + \alpha\Omega_c^2/[4\Delta(\alpha - 1)]$.

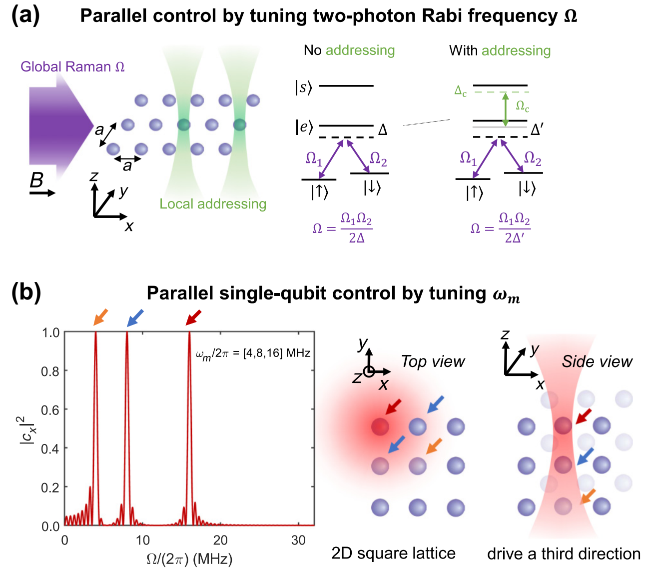

FIG. 4. Two parallel control schemes. (a) Parallel control of an atom array by tuning Ω with additional light shifts. Global qubit operation beams are sent towards atoms to drive a Raman transition between the two qubit states. Individual-addressing beams couple the intermediate state towards another state to induce ac Stark energy shift. (b) Parallel control of an atom array with multiple modulation frequencies. In the simulation we set $\epsilon_m/(2\pi) = 0.125$ MHz; the maximum driving strength of the laser is $\Omega/(2\pi) = 16$ MHz. We show two exemplary application scenarios: a small set of atoms forming a two-dimensional square lattice, and the third direction of a three-dimensional atom array. For the former case, the beam is centered on the atom at the left top corner. One can also choose a lower-symmetry point as the focus center to better differentiate different qubits in practical applications. For the latter case, the beam is applied along the third direction of the array.

We now consider two practical examples in alkaline-earth(like) (^{171}Yb) and alkali (^{87}Rb) atoms to estimate the experimental parameters required to engineer the parallel control scheme assisted by additional addressing light [Fig. 4(a)]. We account for two major noise sources: frequency shifts caused by the AODs (SLMs and DMDs do not have this issue) and incoherent scattering by the intermediate states.

In the case of ^{171}Yb, with the two hyperfine ground states coupled through the triplet clock state $^3P_0$, the fourth level can be the $^3D_1$ state. Undesirable position-dependent frequency shifts δ_c caused by the AOD can lead to a Rabi-frequency change with a ratio $-[4\Delta(1-\alpha)^2/\Omega_c^2]\delta_c$. With parameters $(\Delta, \Omega, \Omega_c, \Delta_c) = (2\pi) \times (10, 1, 40, 70)$ MHz, the Rabi frequency of atoms with the addressing beam is two times larger than for other sites. For a frequency drift $\delta_c/(2\pi)$ across 10 lattice sites from -2.5 to 2.5 MHz [40], the induced infidelity is on the order of 0.2%. The scattering error under this setting is estimated to be on the level of 0.1%.

In the case of ^{87}Rb, we use the two clock states in the hyperfine ground state as the qubit, while the two excited states can be $5^2P_{1/2}$ and $4^2D_{3/2}$, with a transition wavelength of 1475.6 nm. Because of the large linewidth of the intermediate state $5^2P_{1/2}$ (5.75 MHz), the scattering error is the dominant effect and a large detuning Δ on the order of 10–100 GHz is typically used to ensure infidelity to be below 0.1% [5,15]. For a set of practically realizable parameters $(\Delta, \Omega, \Omega_c, \Delta_c) = (2\pi) \times (50, 0.6, 40, -34)$ GHz, the Rabi frequency of atoms with the addressing beam is two times larger than for other sites. The power required for each local addressing beam is 8 mW assuming a beam waist of 2 µm.

We note that, in a practical experimental setting for clock qubits based on alkali atoms, it is preferred to apply the beam along the quantization axis [5] to optimize the ratio between Rabi frequency and intermediate-state scattering. For existing local control demonstrations with individual Raman beams applied perpendicular to the quantization axis, careful calibrations and pulse shaping are needed [15], and a combination of local $Z(\theta)$ and global $\pi/2$ rotations was used to apply local $X(\theta)$ gates [15]. Our scheme is naturally compatible with a global Raman beam sent along the quantization axis to optimize the Rabi frequency and local addressing beams sent perpendicular to the plane of the atom array without introducing new complexities. Moreover, the local addressing beams in our scheme mainly shift the excited states of atoms and leave the qubit space in the ground state less affected. Compared to the typical Stark shift method directly applied to qubit levels, our scheme does not introduce additional decoherence.

B. Parallel control by adding multiple modulations

So far we have demonstrated that, by illuminating a large-size laser beam on a group of atoms, we can selectively drive one target qubit at a different site by tuning the modulation frequency ω_m to the corresponding Rabi frequency $\omega_m = \Omega(r)$, which are controlled either directly by laser intensity for optical qubits or by applying additional light shifts for hyperfine qubits. Actually, the developed scheme can further achieve individual control over a set of target qubits in a highly efficient and parallel manner. Instead of sequentially applying each PM gate with evolution described by Eq. (2), we can engineer phase-modulated driving with multiple modulation frequencies described by

$$\Omega(r)\cos\left(\omega t + \phi - \sum_{i=1}^{n} \frac{2\epsilon_m^{(i)}}{\omega_m^{(i)}} \sin\left(\omega_m^{(i)} t + \phi_m^{(i)}\right)\right)$$

such that the Hamiltonian in the rotating frame is

$$\mathcal{H}_I^{(\mathrm{par})} = \frac{\Omega}{2}\sigma_x' + \sum_{i=1}^{n} \epsilon_m^{(i)} \cos\left(\omega_m^{(i)} t + \phi_m^{(i)}\right)\sigma_z. \qquad (5)$$

The modulation frequency $\omega_m^{(i)}$ is set to match the driving amplitude at site $\Omega(r^{(i)}) = \omega_m^{(i)}$ for all target sites (i) where parallel gates are desired. The modulation frequencies need to satisfy the condition $\omega_m^{(i)} = (2\pi k^{(i)}/\varphi^{(i)})\epsilon_m^{(i)}$, with $k^{(i)}$ integer numbers, to engineer a φ rotation for sites (i). For example, to engineer π rotations for different sites with the same total phase modulation time, $\epsilon_m^{(i)} = \epsilon_m = \pi/T$ for any i and should be chosen as the common divisors of different $\Omega(r^{(i)})$, which slows down the gate speed. We note that such a slowdown is partially made up by the parallelism of the method, and the scenarios where atoms are arranged in a special lattice structure such that both the gate design and the crosstalk suppression become easier to achieve. Moreover, phase modulation devices usually have much faster switching speeds, showing advantages in achieving fast control in atom-array quantum platforms.

In Fig. 4(b), we use numerical simulations to demonstrate the feasibility of such a parallel control technique applied to a small group of atoms. For example, for a small set of atoms arranged in a two-dimensional (2D) square lattice configuration, as shown in Fig. 4(b), we can apply a broad beam centered at the corner of the lattice and simultaneously turn on several modulation frequencies matching the Rabi frequencies of the nearest-neighbor and next-nearest-neighbor sites. As shown by the simulation in Fig. 4(b), an X gate is applied to the corresponding sites indicated by the arrows.

The phase modulation scheme we develop is also useful to control a three-dimensional (3D) atom array when crosstalk effects in the third (z) dimension are even larger (or unavoidable) than in the 2D case. As shown in Fig. 4(b), an exemplary configuration is to apply the control beam along the third dimension of the atom array such that different layers experience different Rabi frequencies. Selective and parallel control can be implemented by switching on several modulation frequencies matching the corresponding Rabi frequencies, as we have introduced.

More generally, to control more atoms in parallel, one can move the beam center to a low-symmetry spatial point such that all sites have different and distinguishable driving amplitudes. To selectively control a subset of atoms in the array, one can switch on their corresponding phase modulation frequencies (matching their driving amplitudes, respectively). Still, with the necessary slowdown of the gate speed, such a control scheme is more favored for controlling a small-scale atom array with a loosely focused beam. For the control of a large-scale atom array, it would be better to combine it with existing parallel control strategies. For example, one can use an AOD to generate a large array of control beams with each of them controlling a small "zone" consisting of either a small set of atoms in 2D or an array of atoms in the third dimension of a 3D atom array.

IV. AVENUES FOR PERFORMANCE IMPROVEMENT

The performance of the crosstalk suppression can be further improved by concatenating the sequence to higher order. For the asymmetric Z gate design in Fig. 2(a), the unitary evolution in the second rotating frame is

$$U^{(1)} = \left[\cos^2\frac{\theta_t}{2} - \sin^2\frac{\theta_t}{2}\sigma_2\cdot\sigma_1\right]I + i\sin^2\frac{\theta_t}{2}[\sigma_1\times\sigma_2] + i\sin\theta_t\frac{\sigma_1+\sigma_2}{2}, \quad (6)$$

where $\theta_t = \epsilon_R t$ is the rotation angle for each half period t with a rate $\epsilon_R = \sqrt{(\Omega-\omega_m)^2+\epsilon_m^2}$, and $\sigma_{1(2)} = (\mp(\Omega-\omega_m)\sigma_x' - \epsilon_m\sigma_z)/\epsilon_R$. We want to achieve an operation $U = -i\sigma_z$ for $\Omega=\omega_m$ ($\sigma_{1,2}=\sigma_z$) and $U\approx I$ for $\Omega,\epsilon_m \ll \omega_m$, such that the crosstalk is suppressed. We note that similar bang-bang sequences have been the object of extensive work in optimal control [41–45].

Our goal is to cancel unwanted terms with sequence concatenation. Since the term $\propto \sigma_1\times\sigma_2$ changes sign with σ_x', it can be canceled by concatenating the sequence with the $0,\pi$ phase alternation. We denote by $\bar{U}^{(1)}$ an evolution similar to $U^{(1)}$ except for a π phase shift in ϕ (and ϕ_m for X gate design) such that the σ_x' term in the Hamiltonian in Eq. (3) switches to $-\sigma_x'$. The symmetric Z gate shown in Fig. 2(a) is actually constructed from the asymmetric one, through unitary $U^{(2)} = \bar{U}^{(1)}U^{(1)}$. Higher-order concatenation can be constructed in the same manner. In Fig. 5, we show the gate improvement through sequence concatenation. As the concatenation order increases, the σ_y or σ_x components in the designed gate become smaller [see Fig. 5(b)]. Meanwhile, the σ_z curve gets more flattened in the center, making the target qubits immune to small driving amplitude fluctuations.

Our gate design is also robust against fluctuations of the frequency detuning. In Figs. 5(c) and 5(d) we show the Z gate fidelity (indicated by the intensity) as a function of both driving amplitude and frequency detuning, where the robustness of our design against both parameters is indicated by the broad regions pointed out by the white arrows.

To suppress crosstalk for a broad range of leakage power, a smaller driving strength ϵ_m is needed, which then makes the gate slower. Such a problem is usually unavoidable in narrowband pulse design since longer evolution is needed to narrow down the "passband." This drawback is partially made up by the enhanced coherence time under

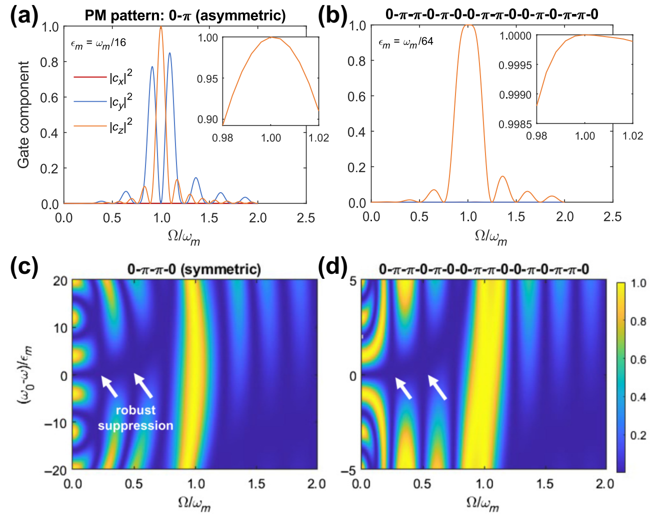

FIG. 5. Gate improvement through sequence concatenation. (a) The components of synthesized Z gate. The phase for the first and second halves are set to $\phi = 0,\pi$. (b) Z gate with a phase pattern $0,\pi,\pi,0,\pi,0,0,\pi,\pi,0,0,\pi,0,\pi,\pi,0$ for 16 equal-duration blocks. (c),(d) 2D maps of the σ_z component as a function of both drive amplitude Ω and detuning $\omega_0-\omega$.

the phase-modulated driving, which makes the qubit insensitive to the dominant low-frequency noise [31]. Moreover, when only the crosstalk on discrete sites needs to be suppressed (e.g., arrays in a lattice structure), we can make use of zero-crossing nodes and avoid choosing small ϵ_m. Although our analysis is based on the RWA, an effective Hamiltonian based on Floquet theory can be used to design the phase pattern analytically with high accuracy beyond the RWA [27,46,47]. To efficiently optimize for discrete or continuous sequence parameters, one could also use numerical optimization methods or machine learning [25,34,48].

We now estimate the fidelity and crosstalk suppression performance of our gate design in a practical scenario with a control beam radius $r_0 = 7$ μm and Rabi frequency $\Omega_0 = (2\pi)2$ MHz [5]. If we consider a single atom with a temperature of 10 μK, the maximum infidelity is 0.001 without any additional phase concatenation. If we consider a worse scenario where a thermal atomic cloud with a radius of 1 μm leads to a Rabi frequency variation of about $1-e^{-1/7^2} = 0.02$, the maximum gate infidelity is 0.1 and can be decreased to below 0.02 by the first-order concatenation design and below 0.001 by the third-order sequence concatenation. For both cases, the crosstalk effect in the nearest-neighbor site for a square lattice is suppressed by more than two orders of magnitude compared to the bare (unmodulated) gate. When compared to beams with a smaller waist and similar sensitivity to the atomic motion, a similar crosstalk suppression performance is expected (see Appendix C). Considering that the intensity spillover is typically higher than in the ideal case (e.g., due to optical aberrations [16]), choosing a larger beam waist combined with our crosstalk suppression scheme can be beneficial with easier alignment and less aberration. Besides, profiling the shape of the beam, for example, with a flat top [49], can also help tackle the trade-off between crosstalk and beam waist.

In the parallel control scheme (Sec. III A), a global beam with a rather uniform intensity (over the whole array) is used and the infidelity due to atomic motion is negligible.

The actual gate infidelity should also account for other error sources, such as the incoherent scattering from intermediate excited states for hyperfine qubits based on alkali atoms. The scattering error scales with the ratio between the scattering rate and two-photon Rabi frequency. Considering the slowdown of the gate speed, the scattering error in our scheme scales as $(\Omega/\epsilon_m)(\Gamma/\Delta)$. By using a large detuning from the intermediate state, allowed by the improved availability of high-power lasers, such infidelity can be suppressed to a level below 0.0001. Under a currently achieved experimental condition [5], we estimate that the scattering error of our scheme is on the order of 0.001. A more detailed calculation is included in Appendix C.

V. DISCUSSION

We developed a phase-modulated control technique to design single-qubit gates that are robust against crosstalk effects due to the leakage of driving power. Strategies including sequence concatenation and hybrid gate design are developed to optimize the robustness against power and frequency fluctuations for the target qubits. Based on the proposed techniques, we use atom arrays as our target systems to develop two parallel single-qubit control schemes by either introducing additional addressing beams, or adding multiple modulation frequencies. Numerical simulations based on experimental parameters are added to show the possibility of implementing our schemes in current platforms.

Typical narrowband composite pulses [22,26,50] could also be used for the crosstalk suppression and the parallel control with additional addressing beams, ideally with similar performance (see Fig. 11 in Appendix A). Our scheme features continuous instead of pulsed operations and is more robust to hardware imperfections such as ring-up (or ring-down) of the pulses, especially when the gate speed becomes faster. The response to the driving amplitude in our design features discrete zero-crossing points at $3/4, 1/2, 1/4, \ldots$, making it compatible with atom arrays with a fixed geometry (e.g., square lattice). Moreover, the capability of adding multiple modulation frequencies in our design enables parallel-gate operations and partially makes up for the slowdown of the gate speed, while existing composite pulses allow only sequential operations. Further improving the gate design by relieving the limitation over the depth $\epsilon_m^{(i)}$ and/or duration of each tone's modulation is of interest for future studies.

Our results provide a new approach for controlling a 3D atom array [51–53]. The current state-of-the-art protocol utilizes two orthogonal crossing beams to apply sufficient light shifts and applies subsequent pulses to cancel the crosstalk effect [36,37]. In contrast, our scheme requires the use of only a single beam and can achieve the crosstalk suppression through phase modulation within a single pulse; thus it is simpler to implement given typical experimental constraints.

In addition, the phase-modulated CCD has been demonstrated to protect the coherence of Rabi oscillation against low-frequency noise [31] and provides benefits in gate fidelity, which is critical in dynamical decoupling applications requiring a large number of single-qubit gates. Further improvement of the gate speed, fidelity, and phase smoothness by introducing more frequency modulations or machine learning is of interest for future research [34]. Although this work focuses on single-qubit gate design for atom arrays, it provides insights in designing two-qubit gate without requiring the slow transport of atoms [9]. The same spirit of differentiating atoms with different frequencies allows the realization of programmable nonlocal interactions [54] and site-selective fast readout [55] in cavity-coupled atom arrays.

The presented technology might be generalized into solid-state quantum platforms such as superconducting (SC) and semiconducting qubits. In particular, control crosstalk in SC qubits [56–59], including crosstalk between dc-bias lines or microwave control lines, has been one of the bottlenecks for scaling up SC-based quantum computers. For qubits whose frequencies are flux-controlled, the coupling from a bias line to an unintended loop and the targeted loop would induce non-negligible fluctuations in the qubit frequencies. This could then require cumbersome error calibration and mitigation processes [58]. The PM technique introduced here could be generalized into controlling the flux of qubits and would help reduce the Z-gate errors.

ACKNOWLEDGMENTS

This work was in part supported by the MIT-Harvard Center for Ultracold Atoms (NSF PHY 1734011) and MISTI Global Seed Funds. G.W. acknowledges Matthew L. Peters and David C. Spierings for helpful discussions.

APPENDIX A: GATE DESIGN WITH PHASE-MODULATED DRIVING

Here we provide further evidence of the performance of our strategies to achieve high-fidelity parallel gates.

In Fig. 6, we show the gate components of the X gate engineered with a single pulse of phase-modulated drive

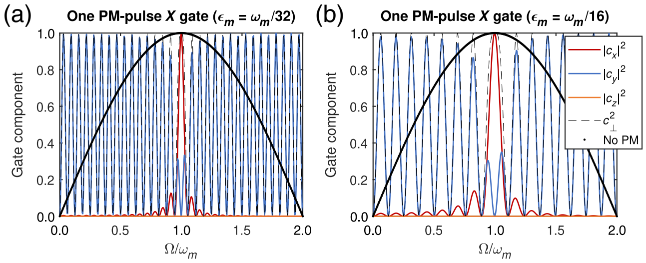

FIG. 6. Direct synthesis of the gate using one PM pulse. The phase is set to $\phi = \pi/2$ and the modulation phase is set to $\phi_m = \pi/2$. The duration of the pulse is set to $T = \pi/\epsilon_m$ and the value of $\epsilon_m = \omega_m/32$ and $\omega_m/16$ for panels (a) and (b), respectively.

without any refocusing. Although the σ_x component is suppressed when $\Omega \ll \omega_m$, a significant amount of σ_y component still exists.

In Fig. 7, we show the gate components of the designed X gate composed of multiple pulses of PM drive under different concatenation orders. Although better performance can be obtained under higher concatenation order, the gate component for $\Omega \ll \omega_m$ is still non-negligible.

In Fig. 8, we show the gate components of the designed X gate based on the hybrid method (PM + normal pulses), which shows nice crosstalk suppression performance, especially under $\Omega \ll \omega_m$. When the order of the concatenation is increased, the unwanted σ_y, σ_z components are better suppressed such that the c_x component at $\Omega/\omega_m = 1$ becomes flatter. However, smaller ϵ_m is needed to maintain a similar profile. Such a trade-off can be further seen in Fig. 9, where we fixed the ϵ_m and find a broader profile when we increase the concatenation order.

We also include the simulation of different gate designs' responses to both the change in driving amplitude Ω and detuning $\omega_0 - \omega$, which are shown in Fig. 10. We can see

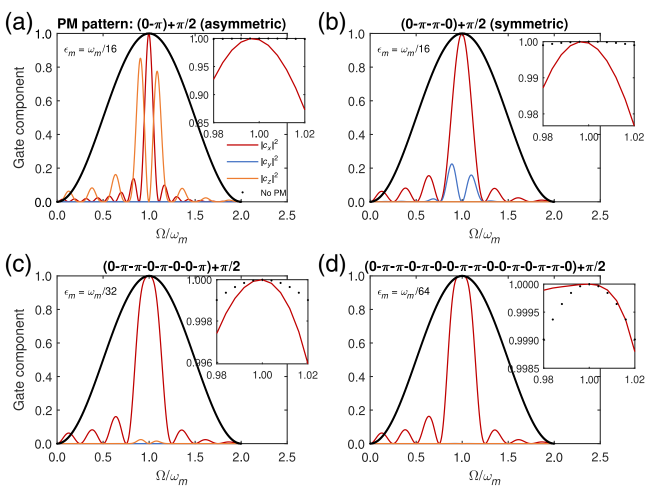

FIG. 7. Comparison of different synthesized X gates (PM design). (a) The phase for the first and second halves are set to $\phi = \pi/2, 3\pi/2$ and $\phi_m = \pi/2, 3\pi/2$, respectively. (b) Similar plot to panel (a) except for the ϕ, ϕ_m phase pattern $\pi/2, 3\pi/2, 3\pi/2, \pi/2$ for four equal-duration blocks. (c) The ϕ, ϕ_m phase pattern is $\pi/2, 3\pi/2, 3\pi/2, \pi/2, 3\pi/2, \pi/2, \pi/2, 3\pi/2$ for eight equal-duration blocks. (d) The ϕ, ϕ_m phase pattern is $\pi/2, 3\pi/2, 3\pi/2, \pi/2, 3\pi/2, \pi/2, \pi/2, 3\pi/2, 3\pi/2, \pi/2, \pi/2, 3\pi/2, \pi/2, 3\pi/2, 3\pi/2, \pi/2$ for 16 equal-duration blocks.

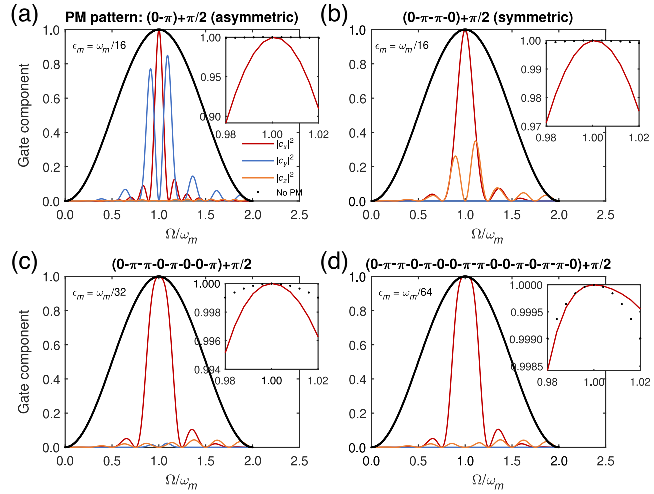

FIG. 8. Comparison of different synthesized X gates (hybrid design). (a) The phase for the first and second halves of the PM Z gate are set to $\phi = 0, \pi$, with the modulation phase set to zero $\phi_m = 0$ [the same for panels (b)–(d)]. (b) Similar plot to panel (a) except for the ϕ phase pattern $0, \pi, \pi, 0$ for four equal-duration blocks. (c) The ϕ phase pattern is $0, \pi, \pi, 0, \pi, 0, 0, \pi$ for eight equal-duration blocks. (d) The ϕ phase pattern is $0, \pi, \pi, \pi, 0, \pi, 0, 0, \pi, \pi, 0, 0, \pi, 0, \pi, \pi, 0$ for 16 equal-duration blocks.

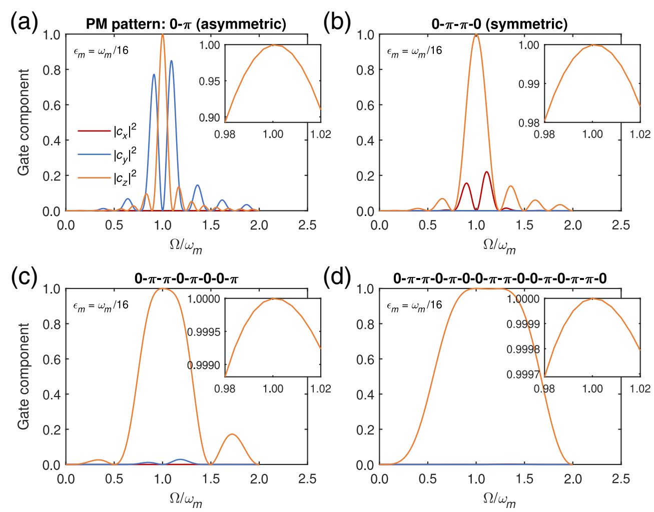

FIG. 9. Comparison of different synthesized Z gates under the fixed modulation strength $\epsilon_m = \omega_m/16$.

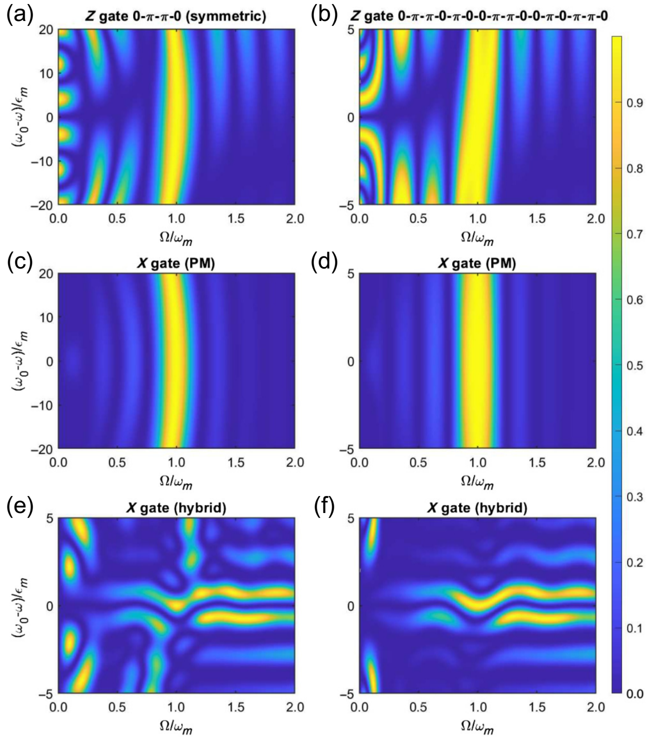

FIG. 10. Comparison of different synthesized Z and X gates. For (a),(c),(e) the modulation strength is set to $\epsilon_m/\omega_m = 1/16$. For (b),(d),(f) the modulation strength is set to $\epsilon_m/\omega_m = 1/64$.

that clear dips are shown in all the gate design cases with different features. For the PM design of the Z gate and X gate, the gate is not sensitive to the detuning and sensitive only to the amplitude change. While for the hybrid design of the X gate, the gate is sensitive to both the detuning and amplitude.

As a comparison to existing composite pulse methods, in Fig. 11 we plot our two X gate designs together with the narrowband (NB) and ultra-narrowband (UNB) designs reported in Refs. [22,26]. We use similar gate speeds (up to the same order of magnitude) for the various methods. The different methods show quite different features, which could be used for different application scenarios. Our method provides nice crosstalk suppression at $\Omega/\omega_m = 3/4, 1/2, 1/4, \ldots$ while sacrificing the smooth feature of the profile in comparison to the NB and UNB methods. We note that combining with numerical optimization and introducing more frequency terms in the phase modulation could provide better performance than our current development, which is out of the focus of this work.

APPENDIX B: PARALLEL CONTROL WITH ADDITIONAL LIGHT SHIFTS

Here we include details on the derivation of the parallel control with individual-addressing control. We consider the four-level energy structure introduced in the main text denoted by $|\uparrow\rangle, |\downarrow\rangle, |e\rangle, |s\rangle$ with energies $-\omega_1, \omega_2, 0, \omega_3$. We apply a circularly polarized drive field with frequencies $\omega_1 + \Delta$, $\omega_2 + \delta + \Delta$, and $\omega_3 + \Delta_c$ to couple the three levels $|\uparrow\rangle, |\downarrow\rangle, |s\rangle$ to the intermediate state $|e\rangle$. The Hamiltonian in the laboratory frame can be written as

$$H = \begin{pmatrix} -\omega_1 & \frac{1}{2}\Omega_1 e^{i(\omega_1+\Delta)t} & 0 & 0 \\ \frac{1}{2}\Omega_1 e^{-i(\omega_1+\Delta)t} & 0 & \frac{1}{2}\Omega_c e^{i(\omega_3+\Delta_c)t} & \frac{1}{2}\Omega_2 e^{-i(\omega_2+\delta+\Delta)t} \\ 0 & \frac{1}{2}\Omega_c e^{-i(\omega_3+\Delta_c)t} & -\omega_3 & 0 \\ 0 & \frac{1}{2}\Omega_2 e^{i(\omega_2+\delta+\Delta)t} & 0 & -\omega_2 \end{pmatrix}. \tag{B1}$$

In a rotating frame defined by $H_0 = \mathrm{diag}(-\omega_1, \Delta, \omega_3 + \Delta_c + \Delta, -\omega_2 - \delta)$, we obtain the Hamiltonian

$$H_I = \begin{pmatrix} 0 & \Omega_1/2 & 0 & 0 \\ \Omega_1/2 & -\Delta & \Omega_c/2 & \Omega_2/2 \\ 0 & \Omega_c/2 & -\Delta-\Delta_c & 0 \\ 0 & \Omega_2/2 & 0 & \delta \end{pmatrix}. \tag{B2}$$

Since the two intermediate states $|e\rangle$ and $|s\rangle$ are mixed with each other due to the additional addressing Ω_c, we develop the following approach to calculate the effective Rabi rate between the two qubit states $|\uparrow\rangle$ and $|\downarrow\rangle$. We define a unitary rotational matrix U_R to diagonalize the space spanned by $|e\rangle, |s\rangle$, which gives rise to a new set of eigenbasis:

$$|\uparrow\rangle = |\uparrow\rangle, \quad |\downarrow\rangle = |\downarrow\rangle \tag{B3}$$

$$|+\rangle = \frac{(\Delta_c - \sqrt{\Delta_c^2 + \Omega_c^2})\,|e\rangle + \Omega_c\,|s\rangle}{\sqrt{(\Delta_c - \sqrt{\Delta_c^2 + \Omega_c^2})^2 + \Omega_c^2}}, \tag{B4}$$

$$|-\rangle = \frac{(\Delta_c + \sqrt{\Delta_c^2 + \Omega_c^2})\,|e\rangle + \Omega_c\,|s\rangle}{\sqrt{(\Delta_c + \sqrt{\Delta_c^2 + \Omega_c^2})^2 + \Omega_c^2}}, \tag{B5}$$

such that the Hamiltonian is given by

$$H_I = U_R H_I U_R^\dagger = \begin{pmatrix} 0 & \Omega_1^+/2 & \Omega_1^-/2 & 0 \\ \Omega_1^+/2 & -\Delta^+ & 0 & \Omega_2^+/2 \\ \Omega_1^-/2 & 0 & -\Delta^- & \Omega_2^-/2 \\ 0 & \Omega_2^+/2 & \Omega_2^-/2 & \delta \end{pmatrix}. \tag{B6}$$

The detunings and driving amplitudes in the new frame are then

$$\Delta^+ = \Delta + \frac{\Delta_c + \sqrt{\Omega_c^2 + \Delta_c^2}}{2}, \tag{B7}$$

$$\Delta^- = \Delta + \frac{\Delta_c - \sqrt{\Omega_c^2 + \Delta_c^2}}{2}, \tag{B8}$$

$$\frac{\Omega_1^+}{\Omega_1} = \frac{\Omega_2^+}{\Omega_2} = \frac{\Delta_c - \sqrt{\Delta_c^2 + \Omega_c^2}}{\sqrt{(\Delta_c - \sqrt{\Delta_c^2 + \Omega_c^2})^2 + \Omega_c^2}}, \tag{B9}$$

$$\frac{\Omega_1^-}{\Omega_1} = \frac{\Omega_2^-}{\Omega_2} = \frac{\Delta_c + \sqrt{\Delta_c^2 + \Omega_c^2}}{\sqrt{(\Delta_c + \sqrt{\Delta_c^2 + \Omega_c^2})^2 + \Omega_c^2}}. \tag{B10}$$

The two-photon Rabi transition between $|\uparrow\rangle$ and $|\downarrow\rangle$ can be mediated by both of the states $|+\rangle$ and $|-\rangle$, while the two transition paths are independent of each other. Thus, the effective Rabi rate is then the sum of the two paths, yielding

$$\begin{aligned} \Omega_{\text{eff}} &= \frac{\Omega_1\Omega_2}{2}\left[\left(\frac{\Omega_1^+}{\Omega_1}\right)^2 \frac{1}{\Delta^+} + \left(\frac{\Omega_1^-}{\Omega_1}\right)^2 \frac{1}{\Delta^-}\right] \\ &= \frac{\Omega_1\Omega_2}{2} \times \frac{4(\Delta+\Delta_c)}{4\Delta(\Delta+\Delta_c) - \Omega_c^2} \\ &= \frac{\Omega_1\Omega_2}{2\Delta - \Omega_c^2/[2(\Delta+\Delta_c)]}. \end{aligned} \tag{B11}$$

If we require the effective Rabi rate for target qubits to be modified by a factor of α in comparison to others without additional addressing Ω_c such that $1/\{\Delta - \Omega_c^2/[4(\Delta+\Delta_c)]\} = \alpha/\Delta$, we can obtain $\Delta_c = -\Delta + \alpha\Omega_c^2/[4\Delta(\alpha-1)]$. For example, to halve the effective Rabi rate with the dressing beam, one can choose the detuning of the individual-addressing beam as $\Delta_c = -\Delta - \Omega_c^2/(4\Delta)$; to double the effective Rabi rate, one can choose $\Delta_c = -\Delta + \Omega_c^2/(2\Delta)$. We implement numerical simulation to validate the effective Rabi rate we derived above. In Fig. 12, we show four cases with $\alpha = 1, 1/2, 4/3, 2$, where the numerical simulation matches the theoretical derivation. Though a very small inconsistency could exist due to the second-order perturbation approximation that we used in deriving the two-photon Rabi rate, numerical simulation is always an efficient way to find out the parameters we need in experiments.

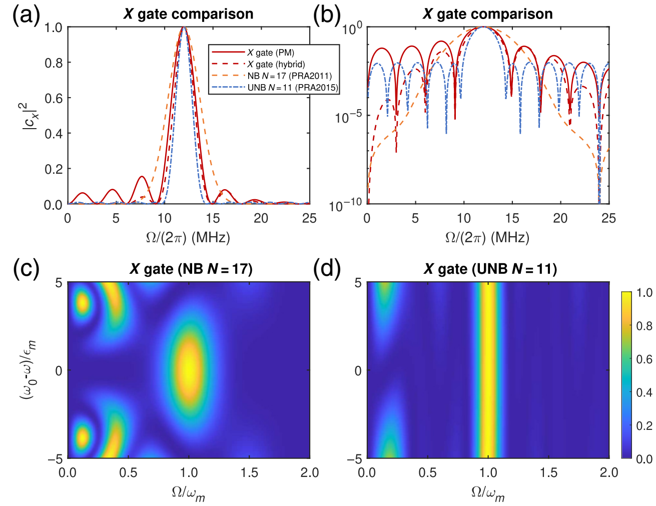

FIG. 11. Comparison to the narrowband composite pulses approach proposed in Refs. [22,26,50].

Next we analyzed the sensitivity to the amplitude of the dressing beam, Ω_c. To achieve arbitrary individual addressing, acousto-optic devices are used, which correlate the positioning of beams to frequency shift. To first order, the relative change of the effective Rabi rate is

$$\frac{\partial\alpha}{\partial\Delta_c}\delta_c = -\frac{4\Delta(1-\alpha)^2}{\Omega_c^2}\delta_c,$$

with δ_c the frequency difference towards the central beam. Therefore, small Δ and large Ω_c are preferred. Here we consider realistic parameters with ^{174}Yb atoms. The two

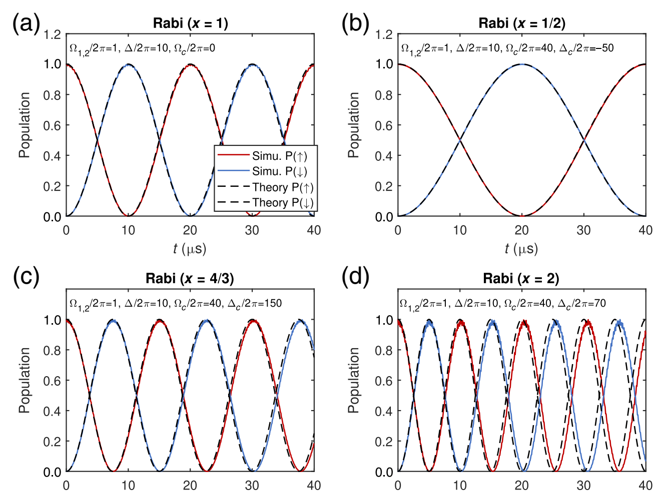

FIG. 12. Tuning two-photon Rabi frequency with detuning Δ_c. The simulation of the time-dependent population on $|\uparrow\rangle$ and $|\downarrow\rangle$ is calculated by directly evolving the system under the Hamiltonian in Eq. (B2). The theoretical predictions shown by the dashed lines are plotted using the effective Rabi rate in Eq. (B11).

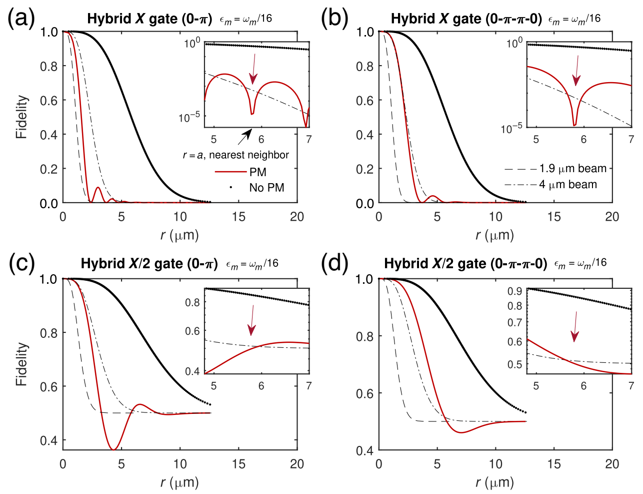

FIG. 13. Gate fidelity and crosstalk suppression effects in a practical setting assuming the radius of the Rabi amplitude profile is $r_0 = 7$ μm. The dashed and dash-dotted lines show the gate fidelity from a tightly focused Raman beam (two-photon control) with a 1.9-μm and 4-μm waist, respectively, without using any phase modulation schemes. (a) Hybrid X gate design with the simplest phase pattern $0, \pi$. (b) Hybrid X gate design with the first-order concatenation of the phase pattern $0, \pi, \pi, 0$. (c) Hybrid $X/2$ gate design with the phase pattern $0, \pi$. (d) Hybrid $X/2$ gate design with the first-order concatenation of the phase pattern $0, \pi, \pi, 0$.

hyperfine ground states of Yb are coupled through the triplet clock state $^3P_0$. The individual-addressing beam couples the transition between the $^3P_0$ and $^3D_1$ states. With $\Delta = (2\pi) \times 10$ MHz, $\Omega = (2\pi) \times 1$ MHz, $\Omega_c = (2\pi) \times 40$ MHz, and $\Delta_c = (2\pi) \times 70$ MHz, the modified Rabi rate with the addressing beam becomes twice the Rabi rate without the addressing beam. The sensitivity towards δ_c is suppressed by a factor of $\Delta/\Omega_c^2 = 1/160$. Here we consider a case similar to that in Ref. [40], in which the frequency drift across 10 lattice sites ranges from $\delta_c = -2.5$ MHz to $\delta_c = 2.5$ MHz; then the infidelity induced by the frequency change is on the order of 0.2%. This infidelity can be mitigated if we calibrate the addressing beam's intensity by adjusting the corresponding radio-frequency power across the array, such that the modified Rabi rate with the addressing beam is uniform.

APPENDIX C: PERFORMANCE ESTIMATION FOR TYPICAL EXPERIMENTAL CONDITIONS

Based on the decomposition of the single-qubit unitary evolution $U = c_0 I + c_x\sigma_x + c_y\sigma_y + c_z\sigma_z$, the process fidelity of the designed Z (X) gate is $F = \mathrm{Tr}|U^\dagger\sigma_z|^2/d^2 = |c_z|^2$ ($|c_x|^2$) with dimension $d = 2$ [60–62]. Thus the process fidelity of the designed gate is conveniently given by the corresponding gate component coefficient.

In general, to improve the performance of crosstalk suppression, one can choose a smaller ϵ_m, which leads to a narrower passband near the resonance condition $\Omega = \omega_m$. However, the narrower passband degrades the gate fidelity when the driving amplitude Ω has effective variations due to either the instability of the laser, or the thermal motion or spatial distribution of the atom (cloud). These variations usually depend on the control beam size, trapping frequency, and temperature. The influence of such variations can be eliminated by improving the passband flatness through sequence concatenation, as introduced in the main text, while a slower gate speed (ϵ_m) is usually needed to ensure a similar narrow bandwidth.

Now we estimate a performance bound of our gate design in a practical scenario. We consider a Rabi spatial profile $\Omega(r) = \Omega_0 e^{-r^2/r_0^2}$ with a radius of $r_0 = 7$ μm, corresponding to a 7-μm (9.9-μm) Gaussian beam waist for single-photon (two-photon) Rabi control. The Rabi frequency is $\Omega_0 = (2\pi) \times 2$ MHz [5] and modulation strength is set to $\epsilon_m = \Omega_0/16$. A single atom cooled to a temperature of 10 μK has a speed of about 44 mm/s (for rubidium) and travels about 0.2 μm within a 4-μs gate duration, leading to a Rabi amplitude variation of up to $1 - e^{-0.2^2/7^2} = 0.0008$. The gate infidelity for the simplest design is upper-bounded to 0.001 without any concatenation. For a worse scenario, we consider an atomic cloud with a radius of 1 μm cooled down to about 10 μK temperature. The spatial variation of atoms dominates the Rabi amplitude variation, which is about $1 - e^{-1/7^2} = 0.02$. The maximum gate infidelity for the simplest design is 0.1 and can be decreased to below 0.02 by the first-order concatenation design and below 0.001 by the third-order sequence concatenation (see Fig. 5 in the main text and Figs. 7–9 in Appendix A).

To better visualize the crosstalk suppression performance at the nearest neighbor for a square lattice, we plot in Fig. 13 the phase-modulated X and $X/2$ gate performance as functions of the distance to the laser beam center r, where we consider the control of an atom array with an interatomic distance of about 6 μm. A large beam with a waist of about 9.9 μm would work in our scheme. The crosstalk effect in the nearest neighbor is suppressed by more than two orders of magnitude compared to the bare gate applied by the same beam. We then compare to the case of bare gates applied by smaller beams, where we consider a 1.9-μm-waist beam (dashed lines) used in Ref. [15] and a 4-μm-waist beam (dash-dotted lines) with similar sensitivity to atomic motion (the curvature at $r = 0$) for a fair comparison. In the comparison, we found that a similar sensitivity to atomic motion would lead to a similar level of crosstalk suppression, though with different details in the profile, as shown by the insets of Fig. 13. Despite such similar trade-offs, a beam with a larger waist (combined with our crosstalk suppression scheme) can still be beneficial since the aberration-induced extra intensity spillover can be worse for smaller-waist beams [16].

The infidelity of a single-qubit gate in actual experiments is also limited by other factors. For hyperfine qubits based on alkaline atoms, such as the clock states of ^{87}Rb, a single-qubit gate is implemented using two-photon Raman transitions mediated by the excited P state. The scattering rate is $\sim(\Omega_d^2/\Delta)\Gamma$ and the two-photon Rabi frequency is $\sim\Omega_d^2/(2\Delta)$. The associated scattering error is then given by their ratio, $\sim\Gamma/\Delta$. Accounting for the slowdown of our control scheme, the scattering error should scale as $\sim(\Omega/\epsilon_m)(\Gamma/\Delta)$. In Ref. [5], the scattering-limited gate infidelity achieved in actual experiments is on the order of 0.0001. Thus, for our scheme, the scattering-limited infidelity should be on the order of 0.001, comparable to other dominant error sources, as we have discussed.

[1] M. Morgado and S. Whitlock, Quantum simulation and computing with Rydberg-interacting qubits, AVS Quantum Sci. **3**, 023501 (2021).
[2] M. Saffman, T. G. Walker, and K. Mølmer, Quantum information with Rydberg atoms, Rev. Mod. Phys. **82**, 2313 (2010).
[3] C. Sheng, X. He, P. Xu, R. Guo, K. Wang, Z. Xiong, M. Liu, J. Wang, and M. Zhan, High-fidelity single-qubit gates on neutral atoms in a two-dimensional magic-intensity optical dipole trap array, Phys. Rev. Lett. **121**, 240501 (2018).
[4] H. Levine, A. Keesling, G. Semeghini, A. Omran, T. T. Wang, S. Ebadi, H. Bernien, M. Greiner, V. Vuletić, H. Pichler, and M. D. Lukin, Parallel implementation of high-fidelity multiqubit gates with neutral atoms, Phys. Rev. Lett. **123**, 170503 (2019).
[5] H. Levine, D. Bluvstein, A. Keesling, T. T. Wang, S. Ebadi, G. Semeghini, A. Omran, M. Greiner, V. Vuletić, and M. D. Lukin, Dispersive optical systems for scalable Raman driving of hyperfine qubits, Phys. Rev. A **105**, 032618 (2022).
[6] S. J. Evered, D. Bluvstein, M. Kalinowski, S. Ebadi, T. Manovitz, H. Zhou, S. H. Li, A. A. Geim, T. T. Wang, N. Maskara, H. Levine, G. Semeghini, M. Greiner, V. Vuletić, and M. D. Lukin, High-fidelity parallel entangling gates on a neutral-atom quantum computer, Nature **622**, 268 (2023).
[7] S. Ma, G. Liu, P. Peng, B. Zhang, S. Jandura, J. Claes, A. P. Burgers, G. Pupillo, S. Puri, and J. D. Thompson, High-fidelity gates and mid-circuit erasure conversion in an atomic qubit, Nature **622**, 279 (2023).
[8] P. Scholl, A. L. Shaw, R. B.-S. Tsai, R. Finkelstein, J. Choi, and M. Endres, Erasure conversion in a high-fidelity Rydberg quantum simulator, Nature **622**, 273 (2023).
[9] D. Bluvstein, H. Levine, G. Semeghini, T. T. Wang, S. Ebadi, M. Kalinowski, A. Keesling, N. Maskara, H. Pichler, M. Greiner, V. Vuletić, and M. D. Lukin, A quantum processor based on coherent transport of entangled atom arrays, Nature **604**, 451 (2022).
[10] A. L. Shaw, R. Finkelstein, R. B.-S. Tsai, P. Scholl, T. H. Yoon, J. Choi, and M. Endres, Multi-ensemble metrology by programming local rotations with atom movements, Nat. Phys. **20**, 195 (2024).
[11] A. Omran, H. Levine, A. Keesling, G. Semeghini, T. T. Wang, S. Ebadi, H. Bernien, A. S. Zibrov, H. Pichler, S. Choi *et al.*, Generation and manipulation of Schrödinger cat states in Rydberg atom arrays, Science **365**, 570 (2019).
[12] H. Labuhn, S. Ravets, D. Barredo, L. Béguin, F. Nogrette, T. Lahaye, and A. Browaeys, Single-atom addressing in microtraps for quantum-state engineering using Rydberg atoms, Phys. Rev. A **90**, 023415 (2014).
[13] S. de Léséleuc, D. Barredo, V. Lienhard, A. Browaeys, and T. Lahaye, Optical control of the resonant dipole-dipole interaction between Rydberg atoms, Phys. Rev. Lett. **119**, 053202 (2017).
[14] A. P. Burgers, S. Ma, S. Saskin, J. Wilson, M. A. Alarcón, C. H. Greene, and J. D. Thompson, Controlling Rydberg excitations using ion-core transitions in alkaline-earth atom-tweezer arrays, PRX Quantum **3**, 020326 (2022).
[15] D. Bluvstein, S. J. Evered, A. A. Geim, S. H. Li, H. Zhou, T. Manovitz, S. Ebadi, M. Cain, M. Kalinowski, D. Hangleiter, J. P. Bonilla Ataides, N. Maskara, I. Cong, X. Gao, P. Sales Rodriguez, T. Karolyshyn, G. Semeghini, M. J. Gullans, M. Greiner, V. Vuletić, and M. D. Lukin, Logical quantum processor based on reconfigurable atom arrays, Nature **626**, 58 (2024).
[16] T. Graham, Y. Song, J. Scott, C. Poole, L. Phuttitarn, K. Jooya, P. Eichler, X. Jiang, A. Marra, B. Grinkemeyer *et al.*, Multi-qubit entanglement and algorithms on a neutral-atom quantum computer, Nature **604**, 457 (2022).
[17] R. Freeman, *Spin Choreography* (Oxford University Press, Oxford, 1998).
[18] K. R. Brown, A. W. Harrow, and I. L. Chuang, Arbitrarily accurate composite pulse sequences, Phys. Rev. A **70**, 052318 (2004).
[19] D. Mc Hugh and J. Twamley, Sixth-order robust gates for quantum control, Phys. Rev. A **71**, 012327 (2005).
[20] B. T. Torosov and N. V. Vitanov, Arbitrarily accurate twin composite π-pulse sequences, Phys. Rev. A **97**, 043408 (2018).
[21] S. Wimperis, Broadband, narrowband, and passband composite pulses for use in advanced NMR experiments, J. Magn. Reson., Ser. A **109**, 221 (1994).
[22] B. T. Torosov, E. S. Kyoseva, and N. V. Vitanov, Composite pulses for ultrabroad-band and ultranarrow-band excitation, Phys. Rev. A **92**, 033406 (2015).
[23] K. Khodjasteh, H. Bluhm, and L. Viola, Automated synthesis of dynamically corrected quantum gates, Phys. Rev. A **86**, 042329 (2012).
[24] K. Khodjasteh and L. Viola, Dynamically error-corrected gates for universal quantum computation, Phys. Rev. Lett. **102**, 080501 (2009).
[25] G. H. Low, T. J. Yoder, and I. L. Chuang, Methodology of resonant equiangular composite quantum gates, Phys. Rev. X **6**, 041067 (2016).
[26] B. T. Torosov and N. V. Vitanov, Smooth composite pulses for high-fidelity quantum information processing, Phys. Rev. A **83**, 053420 (2011).
[27] B. Bartels and F. Mintert, Smooth optimal control with Floquet theory, Phys. Rev. A **88**, 052315 (2013).

[28] J. H. Lee, E. Montano, I. H. Deutsch, and P. S. Jessen, Robust site-resolvable quantum gates in an optical lattice via inhomogeneous control, Nat. Commun. **4**, 2027 (2013).

[29] J.-M. Cai, B. Naydenov, R. Pfeiffer, L. P. McGuinness, K. D. Jahnke, F. Jelezko, M. B. Plenio, and A. Retzker, Robust dynamical decoupling with concatenated continuous driving, New J. Phys. **14**, 113023 (2012).

[30] D. Farfurnik, N. Aharon, I. Cohen, Y. Hovav, A. Retzker, and N. Bar-Gill, Experimental realization of time-dependent phase-modulated continuous dynamical decoupling, Phys. Rev. A **96**, 013850 (2017).

[31] G. Wang, Y.-X. Liu, and P. Cappellaro, Coherence protection and decay mechanism in qubit ensembles under concatenated continuous driving, New J. Phys. **22**, 123045 (2020).

[32] G. Wang, C. Li, and P. Cappellaro, Observation of symmetry-protected selection rules in periodically driven quantum systems, Phys. Rev. Lett. **127**, 140604 (2021).

[33] G. Wang, Y.-X. Liu, and P. Cappellaro, Observation of the high-order Mollow triplet by quantum mode control with concatenated continuous driving, Phys. Rev. A **103**, 022415 (2021).

[34] J. Tian, H. Liu, Y. Liu, P. Yang, R. Betzholz, R. S. Said, F. Jelezko, and J. Cai, Quantum optimal control using phase-modulated driving fields, Phys. Rev. A **102**, 043707 (2020).

[35] N. Khaneja, A. Dubey, and H. S. Atreya, Ultra broadband NMR spectroscopy using multiple rotating frame technique, J. Magn. Reson. **265**, 117 (2016).

[36] Y. Wang, X. Zhang, T. A. Corcovilos, A. Kumar, and D. S. Weiss, Coherent addressing of individual neutral atoms in a 3D optical lattice, Phys. Rev. Lett. **115**, 043003 (2015).

[37] Y. Wang, A. Kumar, T.-Y. Wu, and D. S. Weiss, Single-qubit gates based on targeted phase shifts in a 3D neutral atom array, Science **352**, 1562 (2016).

[38] T. M. Graham, M. Kwon, B. Grinkemeyer, Z. Marra, X. Jiang, M. T. Lichtman, Y. Sun, M. Ebert, and M. Saffman, Rydberg-mediated entanglement in a two-dimensional neutral atom qubit array, Phys. Rev. Lett. **123**, 230501 (2019).

[39] B. Zhang, P. Peng, A. Paul, and J. D. Thompson, Scaled local gate controller for optically addressed qubits, Optica **11**, 227 (2024).

[40] H. Bernien, S. Schwartz, A. Keesling, H. Levine, A. Omran, H. Pichler, S. Choi, A. S. Zibrov, M. Endres, M. Greiner *et al.*, Probing many-body dynamics on a 51-atom quantum simulator, Nature **551**, 579 (2017).

[41] U. Boscain and P. Mason, Time minimal trajectories for a spin 1/2 particle in a magnetic field, J. Math. Phys. **47**, 062101 (2006).

[42] C. D. Aiello, M. Allegra, B. Hemmerling, X. Wan, and P. Cappellaro, Algebraic synthesis of time-optimal unitaries in SU(2) with alternating controls, Quantum Inf. Process. **14**, 3233 (2015).

[43] C. D. Aiello, *Qubit Dynamics under Alternating Controls*, Thesis, Massachusetts Institute of Technology, 2014.

[44] Y. Billig, Optimal attitude control with two rotation axes, SIAM J. Control Optim. **57**, 1068 (2019).

[45] Y. Billig, Time-optimal decompositions in SU(2), Quantum Inf. Process. **12**, 955 (2013).

[46] G. Wang, Y.-X. Liu, J. M. Schloss, S. T. Alsid, D. A. Braje, and P. Cappellaro, Sensing of arbitrary-frequency fields using a quantum mixer, Phys. Rev. X **12**, 021061 (2022).

[47] M. Leskes, P. Madhu, and S. Vega, Floquet theory in solid-state nuclear magnetic resonance, Prog. Nucl. Magn. Reson. Spectrosc. **57**, 345 (2010).

[48] F. Sauvage and F. Mintert, Optimal control of families of quantum gates, Phys. Rev. Lett. **129**, 050507 (2022).

[49] K. Gillen-Christandl, G. D. Gillen, M. J. Piotrowicz, and M. Saffman, Comparison of Gaussian and super Gaussian laser beams for addressing atomic qubits, Appl. Phys. B **122**, 131 (2016).

[50] N. V. Vitanov, Arbitrarily accurate narrowband composite pulse sequences, Phys. Rev. A **84**, 065404 (2011).

[51] D. Barredo, V. Lienhard, S. de Léséleuc, T. Lahaye, and A. Browaeys, Synthetic three-dimensional atomic structures assembled atom by atom, Nature **561**, 79 (2018).

[52] K. D. Nelson, X. Li, and D. S. Weiss, Imaging single atoms in a three-dimensional array, Nat. Phys. **3**, 556 (2007).

[53] A. Kumar, T.-Y. Wu, F. Giraldo, and D. S. Weiss, Sorting ultracold atoms in a three-dimensional optical lattice in a realization of Maxwell's demon, Nature **561**, 83 (2018).

[54] A. Periwal, E. S. Cooper, P. Kunkel, J. F. Wienand, E. J. Davis, and M. Schleier-Smith, Programmable interactions and emergent geometry in an array of atom clouds, Nature **600**, 630 (2021).

[55] B. Hu, J. Sinclair, E. Bytyqi, M. Chong, A. Rudelis, J. Ramette, Z. Vendeiro, and V. Vuletić, Site-selective cavity readout and classical error correction of a 5-bit atomic register, arXiv:2408.15329.

[56] D. M. Abrams, N. Didier, S. A. Caldwell, B. R. Johnson, and C. A. Ryan, Methods for measuring magnetic flux crosstalk between tunable transmons, Phys. Rev. Appl. **12**, 064022 (2019).

[57] C. Rigetti and M. Devoret, Fully microwave-tunable universal gates in superconducting qubits with linear couplings and fixed transition frequencies, Phys. Rev. B **81**, 134507 (2010).

[58] X. Dai, D. Tennant, R. Trappen, A. Martinez, D. Melanson, M. Yurtalan, Y. Tang, S. Novikov, J. Grover, S. Disseler, J. Basham, R. Das, D. Kim, A. Melville, B. Niedzielski, S. Weber, J. Yoder, D. Lidar, and A. Lupascu, Calibration of flux crosstalk in large-scale flux-tunable superconducting quantum circuits, PRX Quantum **2**, 040313 (2021).

[59] Q. Ficheux, L. B. Nguyen, A. Somoroff, H. Xiong, K. N. Nesterov, M. G. Vavilov, and V. E. Manucharyan, Fast logic with slow qubits: Microwave-activated controlled-Z gate on low-frequency fluxoniums, Phys. Rev. X **11**, 021026 (2021).

[60] E. M. Fortunato, M. A. Pravia, N. Boulant, G. Teklemariam, T. F. Havel, and D. G. Cory, Design of strongly modulating pulses to implement precise effective Hamiltonians for quantum information processing, J. Chem. Phys. **116**, 7599 (2002).

[61] J. M. Chow, J. M. Gambetta, L. Tornberg, J. Koch, L. S. Bishop, A. A. Houck, B. R. Johnson, L. Frunzio, S. M. Girvin, and R. J. Schoelkopf, Randomized benchmarking and process tomography for gate errors in a solid-state qubit, Phys. Rev. Lett. **102**, 090502 (2009).

[62] L. H. Pedersen, N. M. Møller, and K. Mølmer, Fidelity of quantum operations, Phys. Lett. A **367**, 47 (2007).